Multilevel Supply-Modulated Chireix Outphasing With Continuous Input Modulation

Tommaso Cappello, *Member, IEEE*, Taylor W. Barton, *Member, IEEE*, Corrado Florian, *Member, IEEE*, Michael Litchfield, *Member, IEEE*, and Zoya Popovic, *Fellow, IEEE*

***Abstract*— This paper presents a dynamic characterization of a multilevel (ML) Chireix outphasing (ML-CO) power amplifier (PA) with modulated signals. The ML-CO technique combines the advantages of envelope tracking and outphasing architectures by limiting the supply modulation to discrete levels with an efficient power-DAC modulator and using outphasing for fine amplitude control. We describe an experimental test bench that supplies the required phase- and time-aligned modulated signals for outphasing and supply modulation simultaneously. Pulsed characterization is used to design an ML memoryless polynomial DPD. The linearized ML-CO GaN X-band MMIC PA is demonstrated with fixed input drive levels for 9.3-dB peak-to-average power ratio (PAPR), 1.4-MHz and 11.3-dB PAPR, 10-MHz LTE signals with a 9.7-GHz carrier. For both signals, the average total power consumption is reduced by a factor of two when supply modulation is used. An investigation of control signal generation strategies is presented, including combinations of discrete supply and continuous input modulation. A simple exponential function tracks the optimal efficiency trajectory of the ML-CO PA, enabling overall efficiency improvements within 9 and 27 percentage points. This control strategy is applied to radar pulses with amplitude shaping and frequency chirp, with the efficiency improvement of up to 11.8 percentage points compared with constant-supply operation, with 29-dB improvement in spectral confinement.**

***Index Terms*— Chireix, high efficiency, LTE, outphasing, power amplifiers (PAs), radar signals, supply modulation.**

I. Introduction

As COMMUNICATIONS systems continue to move toward signals with higher peak-to-average power ratio (PAPR), it is increasingly important for power amplifiers (PAs) to have high efficiency over a wide dynamic range. Efficiency enhancement techniques, such as Doherty [1]–[5], envelope tracking (ET) [6]–[8], and outphasing [9]–[11], have been developed to extend efficient operation into back-off. Individually, however, these techniques may not provide sufficient back-off efficiency for communications signals, especially at high frequencies. The power range over which a PA operates efficiently can be extended by combining multiple efficiency enhancement techniques, whether of the same type as in multiway Doherty [3]–[5] and multiway outphasing [10], [11], or by combining Doherty and outphasing techniques with supply modulation.

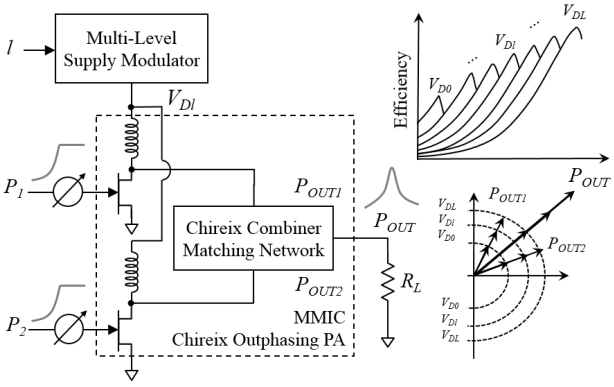

Fig. 1. Simplified diagram of the ML-CO system. This technique uses an ML converter (i.e., power-DAC) to modulate a CO PA [12]. Input power is varied to enhance PA efficiency for every supply voltage level.

Supply modulation extends the dynamic range of a PA by reducing the drain voltage when low output power is needed, and is most commonly implemented as continuous ET [6]. The supply modulator efficiency degrades with increased signal bandwidth, limiting the total transmitter efficiency. This is exacerbated by the 5–10 t imes bandwidth expansion of the ET signal, making continuous tracking effective for narrowband signals only. Techniques that reduce the required supply modulation bandwidth [7], [8], [13], [14] result in reduced linearity.

An alternative to continuous ET is to switch between discrete dc supply levels, which is another type of supply modulator bandwidth reduction approach. By limiting the supply modulation to coarse amplitude control, e.g., with an efficient power-DAC [15], the envelope tracker can be improved compared with a linear tracker. In this approach, a secondary method is used for fine amplitude control between the levels provided by supply modulation. Multilevel (ML) discrete supply modulation has been applied to single-ended PAs [16], dynamically load modulated PAs [17], gate modulation [18], and outphasing PAs with isolating power combiners [19], [20].

In this paper, we use discrete supply modulation in combination with Chireix outphasing (CO) to extend the efficient

Manuscript received July 1, 2017; revised September 7, 2017; accepted September 11, 2017. Date of publication October 4, 2017; date of current version December 12, 2017. This work was supported in part by the Office of Naval Research under Grant N00014-11-1-0931 and in part by Rockwell Collins under Grant 4504348308. This paper is an expanded version from the 2017 International Microwave Conference, Honolulu, HI, USA, June 4–9, 2017. *(Corresponding author: Tommaso Cappello.)*

T. Cappello, T. W. Barton, and Z. Popovic are with the Department of Electrical, Computer, and Energy Engineering, University of Colorado Boulder, Boulder, CO 80309 USA (e-mail: tommaso.cappello@colorado.edu).

C. Florian is with the Department of Electrical, Electronic, and Information Engineering, University of Bologna, Bologna, Italy (e-mail: corrado.florian@unibo.it.

M. Litchfield is with BAE Systems, Nashua, NH 03060 USA.

Color versions of one or more of the figures in this paper are available online at http://ieeexplore.ieee.org.

Digital Object Identifier 10.1109/TMTT.2017.2756038

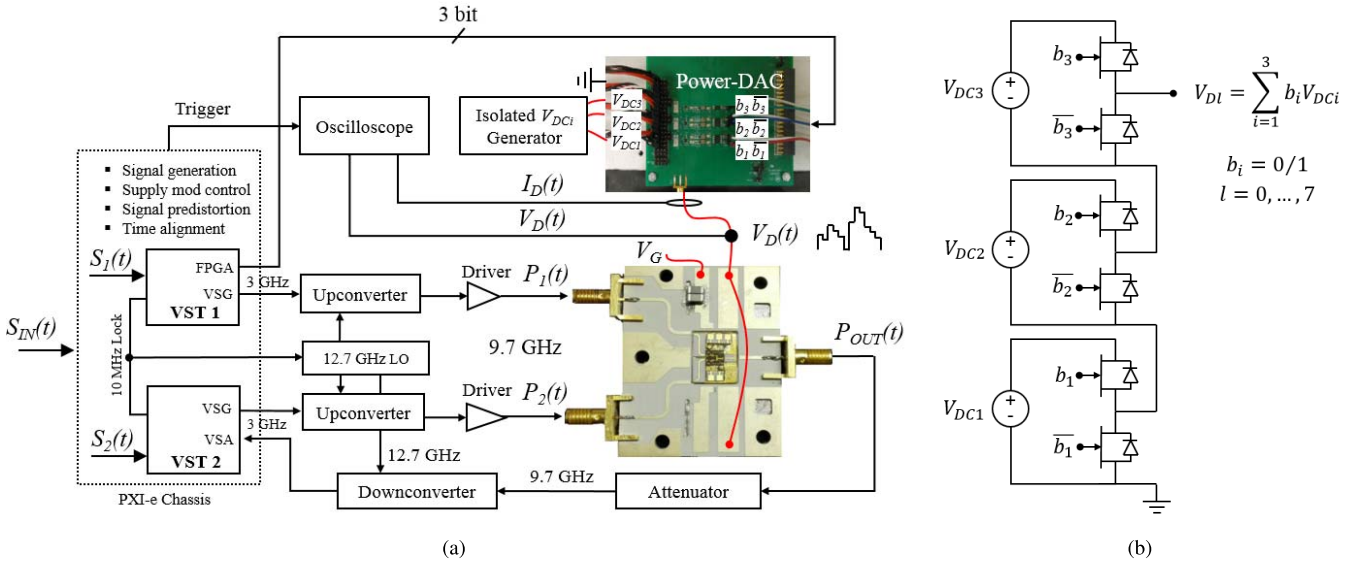

(a) (b)

Fig. 2. (a) Block diagram of the characterization setup based on two NI VSTs (=VSG+VSA) and a hybrid eight-level supply modulator (power-DAC). The PA input signals, $S_1(t)$ and $S_2(t)$, are generated by the VSGs, while the output $S_{\mathrm{OUT}}(t)$ is sampled by a VSA. Drain voltage $V_D(t)$ and current $I_D(t)$ are sensed by a synchronized oscilloscope. External upconversion and downconversion stages are used to modulate $S_1(t)$, $S_2(t)$, and $S_{\mathrm{OUT}}(t)$ at 9.7 GHz. (b) Schematic of the 3-b power-DAC; three half bridges are stacked and controlled by 3 b, b_i, and their complementary, $\overline{b_i}$. Eight voltage levels are generated at the output V_{Dl}, which is connected to the drain of the PA.

operating range of an X-band MMIC PA. A simplified block diagram of the ML CO (ML-CO) architecture is shown in Fig. 1. Compared with ML techniques employing a Wilkinson (isolating) power combiner [19], [20], the fine-amplitude control efficiency is higher due to the lack of an isolation resistor in the power-combining network. ML-CO PAs have previously been demonstrated for CW measurements in [12] and [21]. In the ML-CO architecture, nonlinearities are produced in the load-modulation and envelope modulation paths, and the time alignment between the phase and amplitude control paths is critical to reduce memory effects.

In [22], we demonstrated the modulated signals with this architecture for the first time. The experimental demonstration showed the proof of concept for 10-MHz LTE signals based on a combination of discrete-level supply modulation and constant-amplitude, and phase-modulated inputs to the out-phasing PA. Here, we extend [22] with a detailed investigation of input signal generation and control strategies. A limitation of conventional outphasing with constant-amplitude drive is the gain degradation that occurs at low power levels [23]–[25], which is further degraded with supply modulation, affecting linearity and PAE. Drive amplitude modulation is introduced, in this paper, to improve transmitter performance. The PA is characterized under multiple control strategies, resulting in a shaping function for amplitude control of the ML-CO PA, which demonstrates the efficiency and linearity improvements for amplitude-modulated chirped radar pulses.

The remainder of this paper is organized as follows. In Section II, we describe the ML-CO system and test bench used to validate the approach, including the details of baseband signal generation and characterization of the PA using a pulse sequence and a preliminary validation with broadband LTE signals. Section III introduces the four control strategies considered in this paper, with a comparison of efficiency, complexity, and linearity, and the details of the proposed exponential mapping function for continuous input modulation. In Section IV, the control strategy is applied to radar signals, for which amplitude shaping is used to reduce spectral occupancy. Conclusions are drawn in Section V.

II. Measurement Setup

A detailed block diagram of the ML-CO architecture is shown in Fig. 2(a). The PA MMIC is fabricated in Qorvo's 0.15-μm GaN-on-SiC process and designed to operate in class F with 37 dBm (5 W) CW output power at 9.7 GHz [26]. The breakdown voltage of this process is 50 V, and the PA MMIC is designed for a nominal supply voltage of 20 V, with a drain current of 10 mA for a fixed gate bias voltage at pinchoff $V_{\mathrm{GS,TH}} = -3.5$ V. The Chireix power combiner performs both fundamental matching and phase-dependent load modulation [12]. The CO PA has been designed to be supply modulated with no need of external stability capacitors, and only a 20-pF metal–insulator–metal capacitor is present on the MMIC.

The GaN MMIC is mounted on a CuMo fixture and accessed by 50-Ω microstrip lines on alumina. The fixture is hosted on an external mounting board implemented on a low-loss Roger TMM10i substrate, which provides transitions to SMA connectors, and gate and drain bias pads. The supply modulator is directly connected to the PA board and a bond wire is employed as an air bridge to connect the drains of the two PAs on the MMIC.

The hybrid ML discrete supply modulator is based on a 3-b power-DAC architecture [see Fig. 2(b)] that has been demonstrated to effectively modulate an L-band hybrid LDMOS PA with high-PAPR communication signals [15] and an X-band

GaN MMIC PA driven with arbitrary pulses for radar applications [27]. This supply modulator implements the binary summation of three isolated input voltage sources $V_{\mathrm{DC1}} = 11.2$ V, $V_{\mathrm{DC2}} = 5.6$ V, and $V_{\mathrm{DC3}} = 3.2$ V to generate $L = 2^3 - 1$ (one level is zero) voltage levels as

$$V_{Dl} = \sum_{i=1}^{3} b_i V_{\mathrm{DCi}} \tag{1}$$

$$V_{D7} = V_{D,\mathrm{MAX}} = V_{\mathrm{DC1}} + V_{\mathrm{DC2}} + V_{\mathrm{DC3}} = 20\ \mathrm{V}. \tag{2}$$

The power-DAC output voltage V_{Dl}, with $l = 0, \ldots, L$, can cover the whole dynamic range 0–20 V with high resolution (about 3.2 V). Thanks to the high figure of merit of the power switches [28], this supply modulator achieves 95% efficiency for signals with hundreds of kilohertz bandwidths [27], while 92% and 83% have been obtained, respectively, for 1.4- and 10-MHz LTE signals [15]. The total efficiency $\eta_{\mathrm{TOT,SYS}}$ of the ML-CO architecture can be defined as

$$\eta_{\mathrm{TOT,SYS}} = \eta_{pDAC} \cdot \eta_{\mathrm{TOT,PA}}. \tag{3}$$

Because of the high efficiency of the supply tracker (a key advantage of discrete supply modulation compared with continuous linear tracking), the total efficiency of the system is dominated by the PA efficiency.

A major challenge in modulated outphasing testing is the need to generate multiple dynamic phase- and time-aligned drive signals for the two PAs and for the supply modulator. To this aim, we use two National Instrument Vector Signal Transceivers (NI VST 5644R) with 80-MHz analog bandwidth, phase-locked by the PXI-express bus. Prior to generation, any type of digital modulation can be applied to the I/Q signals in the two VSTs. These signals are then generated at digital baseband and upconverted at first at 3 GHz by the VSTs. Subsequently, the outputs from the VSTs are upconverted to the 9.7-GHz operating frequency of the PAs. The two X-band upconverters are realized with off-the-shelves double-balanced diode mixers (Mini-Circuits ZX05-153MH+) followed by image-rejection filters (K&L Microwave 4ED10-10500). Two benchtop drivers (Mini-Circuits ZVE-3W-183+) are used to amplify the upconverter outputs to the designed PA input power of 25 dBm. Symmetric components have been selected in order to minimize amplitude and phase imbalances between the two branches. However, an unavoidable variation between the two branches has been observed and corrected in the digital baseband.

Similarly, the ML-CO PA output is downconverted in two steps. The PA output is first attenuated (40 dB) and downconverted at 3 GHz by a double-balanced mixer (Mini-Circuits ZX05-153MH+) and low-pass filter, which selects the useful IF component at 3 GHz. The final conversion to digital baseband is directly performed within the VST.

The external LO used for upconversion generates CW power at 12.7 GHz and is also phase-locked to the 10-MHz reference clock of the VSTs. The LO output is split in three ways to feed the two upconverters and the downconverter. Two power splitters (Mini-Circuits ZFRSC-183+) are employed for this purpose. Simultaneously, a time-aligned digital signal

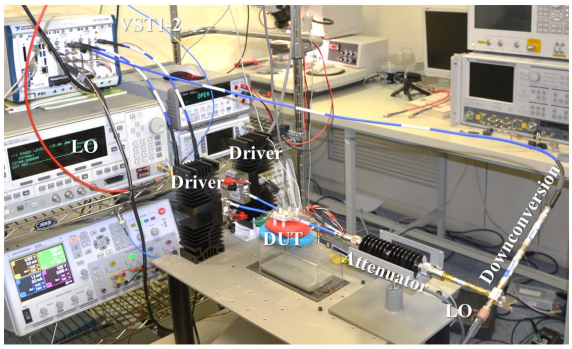

Fig. 3. Photograph of the setup (oscilloscope not visible).

generated by the FPGA integrated in the VST controls the supply modulator and triggers the oscilloscope acquisition of drain voltage $V_D(t)$ and current $I_D(t)$. The setup is calibrated at the inputs and output RF bond pads on the GaN MMIC. A photograph of the setup is shown in Fig. 3.

A. Digital Baseband

The block diagram of the digital baseband is shown in Fig. 4. The digital equivalent of the input signal $S_{\mathrm{IN}}(t)$ of the transmitter is expressed generally as

$$S_{\mathrm{IN}} = Ae^{j\phi}. \tag{4}$$

S_{IN} is then decomposed by a signal component separator into two constant-envelope signals $e^{j(\phi+\theta)}$ and $e^{j(\phi-\theta)}$ with outphasing angle θ defined as

$$\theta = \cos^{-1}(A). \tag{5}$$

Depending on the active supply level l, amplitude modulation can be applied to the exponentials as $K_l(A)e^{j(\phi+\theta)}$ and $K_l(A)e^{j(\phi-\theta)}$. Complex multipliers could be used for this purpose.

In case of fixed input power outphasing ($K_l(A) = 1$), these amplitude-modulated signals reduce to constant-envelope signals, and the setup generates $P_1 = P_2 = 25$ dBm of CW power. If amplitude modulation is employed to reduce input power for efficiency, $K_l(A)$ is varied accordingly by means of an input shaping function, which is extracted during the PA characterization phase. This input shaping function maps the optimal $K_l(A)$ amplitude for the given input power (or A) and supply level $l = 0, \ldots, L$.

A dynamic ML characterization is used to determine the ML-CO characteristics, and the shaping function for the supply modulation and the characterization sequence is shown in Fig. 6(a).

As in [15] and [27], an ML memoryless polynomial DPD is employed between the global input S_{IN} and output S_{OUT} of the transmitter. This DPD approach is reproduced as (6)–(8) here, where $S_{\mathrm{IN}}(n)$ is the digital equivalent of $S_{\mathrm{IN}}(t)$ and $S_{\mathrm{DPD}}(n)$ is the baseband predistorter output, and $\mathscr{F}_D$ is the supply shaping function. The complex coefficients $a_{k,l}$ depend on the instantaneous bias voltage V_{Dl} and on the order of the

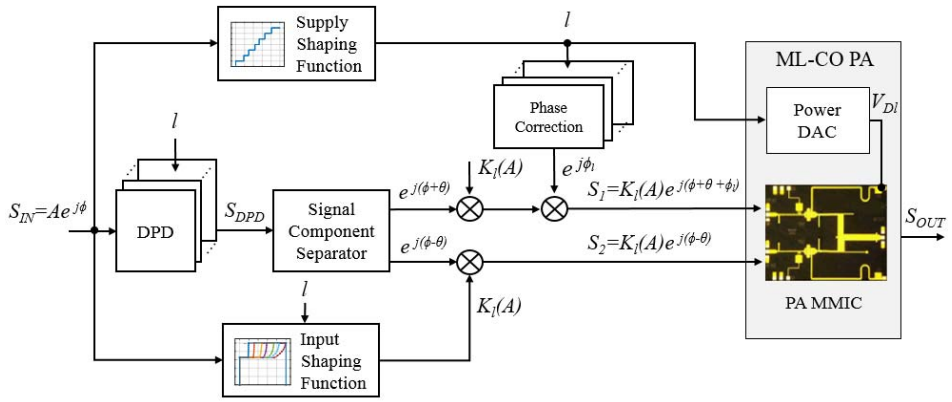

Fig. 4. Block diagram of the digital baseband. The input signal S_{IN} is predistorted (DPD) and it feeds a signal component separator, which generates two constant-envelope signals with differential phase, θ. A supply shaping function generates the lth level controlling the power-DAC, the DPD, the phase correction, and the input shaping function. Drive modulation $K_l(A)$ is introduced on both branches for intralevel efficiency improvement. The complex modulated signal S_{OUT} is reconstructed at the output of the Chireix combiner.

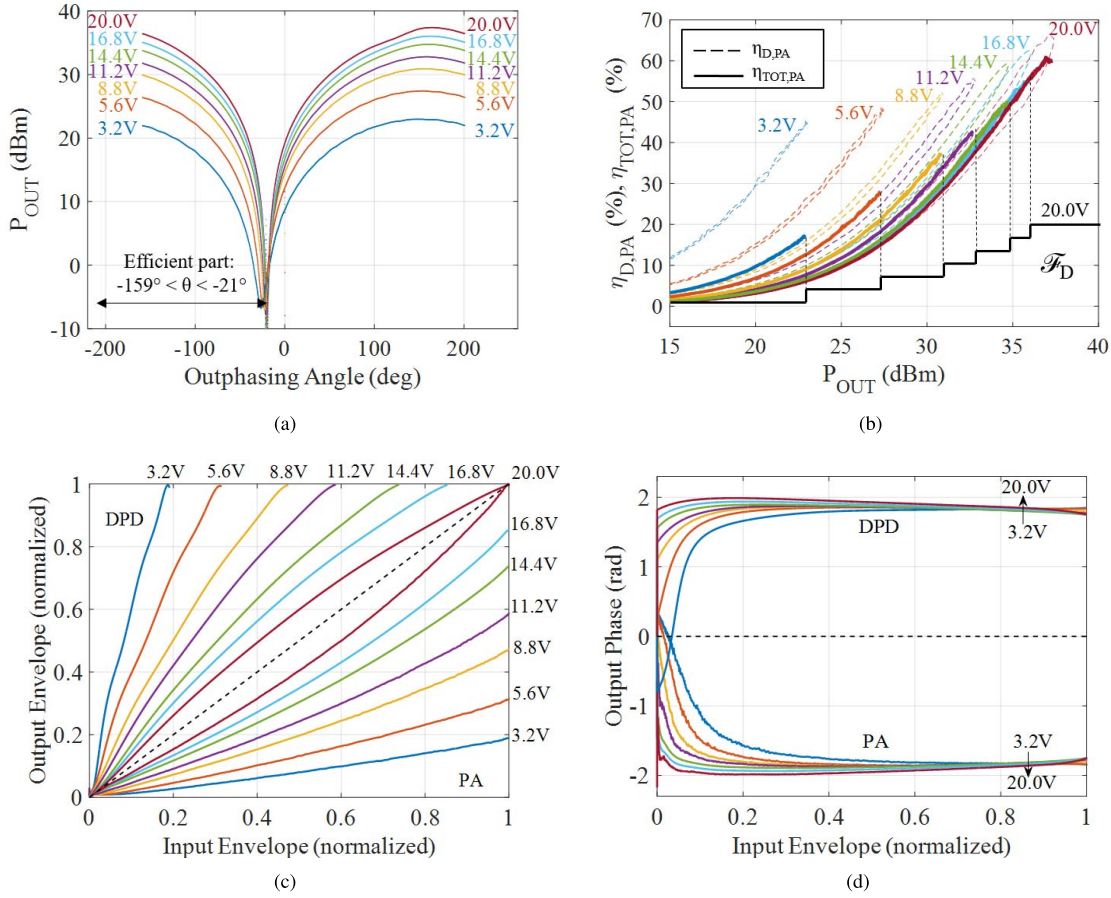

Fig. 5. Characterization results of the ML-CO PA operating at 9.7 GHz and with 25-dBm input power. (a) Outphasing behavior is shown for a complete phase sweep. (b) Total efficiency $\eta_{\mathrm{TOT,PA}}$ is compared with drain efficiency $\eta_{D,\mathrm{PA}}$, and the supply shaping function $\mathscr{F}_D$ is also shown in the plot. (c) AM/AM characteristics. (d) AM/PM characteristics.

polynomial ($K_l = 9$). For every supply level $l = 1, \ldots, L$, the predistorter output can be obtained as

$$S_{\mathrm{DPD}}(n) = \sum_{k=1}^{K_l} a_{k,l} S_{\mathrm{IN}}(n)|S_{\mathrm{IN}}(n)|^{k-1} \tag{6}$$

$$a_{k,l} = |a_{k,l}|e^{j\angle a_{k,l}} = a_{k,l}(V_{Dl}) \tag{7}$$

$$V_{Dl} = \mathscr{F}_D(|S_{\mathrm{IN}}(n)|). \tag{8}$$

The model coefficients are determined by complex polynomial fitting of the inverse of the measured PA characteristics at each l bias levels, as shown in Fig. 5(c) and (d) along with the DPD correction corresponding to each supply level. Note that only the most efficient part of the outphasing angle ($-159° < \theta < -21°$) has been considered hereafter in this paper, which corresponds to the upper part of the efficiency loops [Fig. 5(b)] and to the left part of the P_{OUT} versus θ

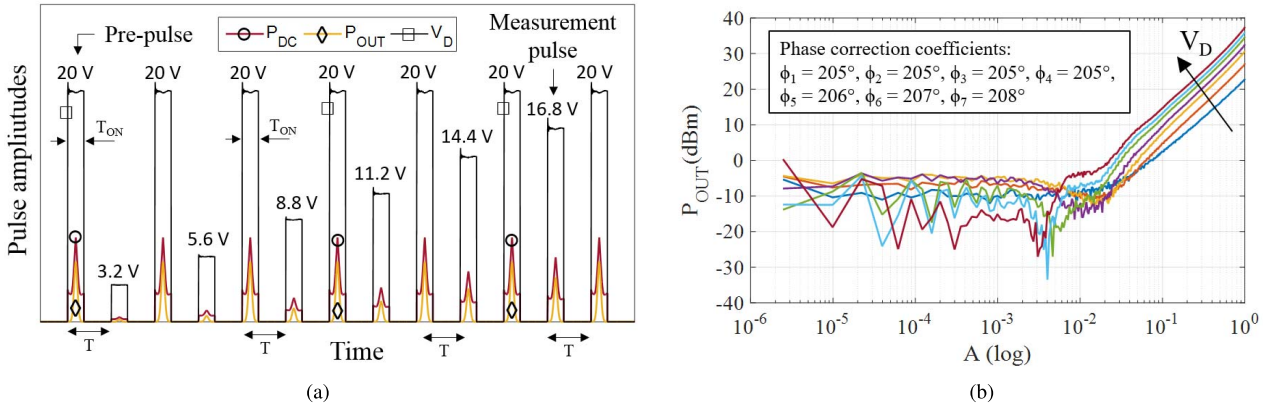

Fig. 6. Characterization results of the ML-CO PA. (a) Pulse sequence used to extract the nonlinear characteristics of the PA; a pulse duration $T_{\rm ON} = 10\ \mu$s and a pulse repetition period $T = 100\ \mu$s are selected. Note that the horizontal axis is not to scale, since $T \gg T_{\rm ON}$. (b) Details of the "small signal" performance of the ML-CO PA with 25-dBm constant input power and phase correction coefficients applied in the digital baseband.

characteristics shown in Fig. 5(a). In this way, the AM/AM and AM/PM characteristics clearly show a single trajectory (without hysteresis) that can be fit with a memoryless polynomial. We note that the biggest efficiency loop is observed at $V_{D7} = 20$ V, and the loops tend to disappear at lower drain voltages. This behavior is also confirmed by CW measurements of the same CO PA in [26]. This effect can be explained by considering that the integrated Chireix combiner is optimized in the PA design for $V_{D7} = 20$ V to provide the maximum output power, and not for lower V_D values. At lower supply voltages, the output impedance of the HEMT devices [i.e., $C_{\rm DS}(V_{\rm DS})$] is varied, and the load modulation effect is less marked as can be appreciated in Fig. 5(b) and in [26].

The supply shaping function $\mathcal{F}_D$ is selected to maximize efficiency for the whole output power range. The peak output power within each supply level defines the thresholds for the commutation between the V_{Dl} levels of the power-DAC, as shown in Fig. 5(b).

Channel equalization is verified during the calibration phase of the bench with a power meter, which showed amplitude imbalances less than 0.1 dB after 30 min warm-up time. For the phase imbalances between the two branches, the pulsed characterization of the PA is employed to empirically extract the $L = 7$ correction coefficients e^{ϕ_l} for any supply level and peak input power of the lth level. Indeed, these correction coefficients depend on both the input power (typically 25 dBm, but can be varied with amplitude modulation) and the supply level, which can alter both the combining phase imbalance and the input match.

These correction coefficients ϕ_l are applied to one of the two branches in the digital baseband. Only phase calibration has been observed to be beneficial. In summary, the resulting digital signals can be expressed as

$$S_1 = K_l(A)e^{j(\phi+\theta+\phi_l)} \tag{9}$$

$$S_2 = K_l(A)e^{j(\phi-\theta)}. \tag{10}$$

The effect of this ML phase correction can be observed in Fig. 6(b) for all the different bias levels and with the phase coefficients reported in the plot inset. With 25-dBm peak input power, the presented setup and PA achieve an output power dynamic range between −4 and 37 dBm. Lower output power values can be achieved by decreasing the input power, which has been kept 25 dBm for this experiment.

The I/Q components of the signals S_1 and S_2 are obtained by off-line computation in MATLAB and are stored in the memory of the VSTs. A LabVIEW software controls the setup, the signal generation, and the acquisition of the PA output $S_{\rm OUT}$. A custom firmware has been developed and mapped on the FPGA of the VST 1 containing an auxiliary memory for the real-time power-DAC control.

B. Characterization With Fixed Input Power

A preliminary static characterization of the ML-CO PA is reported in [26]. The ML-CO PA is first characterized over multiple supply levels using pulses at fixed power level (25 dBm). Phase modulation is introduced between the two signals S_1 and S_2 by varying the outphasing angle θ and by considering an input signal $S_{\rm IN}$ with amplitude modulation (Blackman window) and a pulse duration $T_{\rm ON} = 10\ \mu$s with repetition period $T = 100\ \mu$s. The measured output power, dc power consumption, and supply voltage are shown in Fig. 6(a).

In order to extract an accurate description of the PA with the actual working condition, a pulsed characterization technique [29] is employed. In such a technique, a prepulse at 20 V sets the traps of the GaN PA to a known state, and this prepulse is followed by the actual measurement pulse to extract the nonlinear behavior of the PA for every supply voltage levels, as qualitatively shown in Fig. 6(a). Through this technique, the thermal state of the PA can be adjusted by varying the duration of the prepulse and of the measurement pulse [15], [29], [30].

The outphasing behavior is characterized based on these pulsed measurements and is shown in Fig. 5(a). In [22], drain efficiency $\eta_{D,\rm PA}$ was considered and here reported in Fig. 5(b). However, total efficiency is typically quoted in the outphasing literature whose definition is here reported

$$\eta_{\rm TOT,PA} = \frac{P_{\rm OUT}}{P_{\rm DC} + P_1 + P_2}. \tag{11}$$

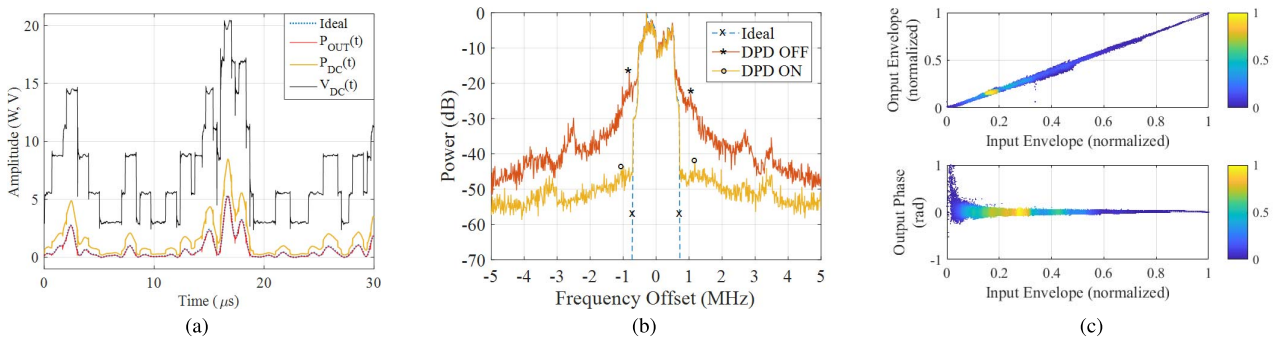

Fig. 7. (a) Exemplifying time-domain waveforms and (b) spectra for the LTE downlink channel at 1.4-MHz and 9.3-dB PAPR. (c) Dynamic AM/AM and AM/PM characteristics with DPD enabled.

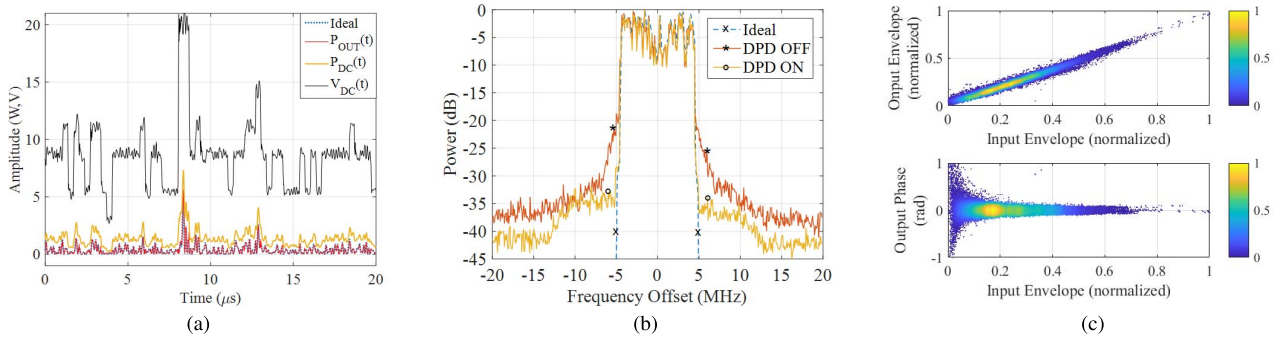

Fig. 8. (a) Exemplifying time-domain waveforms and (b) spectra for the LTE downlink channel at 10-MHz and 11.3-dB PAPR. (c) Dynamic AM/AM and AM/PM characteristics with DPD enabled.

TABLE I
PERFORMANCE SUMMARY WITH LTE SIGNALS

Signal (PAPR)	Control Strategy	EVM	ACLR	P_{DC}	P_{OUT}	P_{IN}	$\eta_{D,PA}$	$\eta_{TOT,PA}$	η_{pDAC}	$\eta_{D,SYS}$	$\eta_{TOT,SYS}$
LTE 1.4 MHz (9.3 dB)	Fixed Bias w/ DPD	2.6%	-47.2 dB	2.80 W	0.54 W	0.63 W	19.3%	15.7%	-	19.3%	15.7%
LTE 1.4 MHz (9.3 dB)	**Supply Mod. w/ DPD**	**4.7%**	**-41.6 dB**	**1.42 W**	**0.54 W**	**0.63 W**	**38.0%**	**26.3%**	**93%**	**38.0%**	**24.5%**
LTE 10 MHz (11.3 dB)	Fixed Bias w/ DPD	4.7%	-39.0 dB	2.62 W	0.35 W	0.63 W	13.4%	10.8%	-	13.4%	10.8%
LTE 10 MHz (11.3 dB)	**Supply Mod. w/ DPD**	**7%**	**-31.5 dB**	**1.37 W**	**0.35 W**	**0.63 W**	**25.6%**	**17.5%**	**89%**	**25.6%**	**15.6%**

When the input power is taken into account, a significant reduction in the efficiency is noticeable [see Fig. 5(b)]. The efficiency trajectories are employed to generate the supply shaping function, which is highlighted in Fig. 5(b).

In the next section, a continuous amplitude modulation of the PA inputs (easily implemented with the proposed setup) will be used to enhance back-off efficiency.

C. Experimental Results

With the test bench and DPD fully characterized as described earlier, this setup is demonstrated at first using LTE signals. Figs. 7(a) and 8(a) show the time-domain signal decomposition with ET. The outphasing signals (not shown) are used to compensate for the discrete steps of the supply voltage V_{Dl} to obtain a continuous output signal P_{OUT}. The dc power consumption P_{DC} is reduced by ML supply modulation. The nonperfect cancellation of the discontinuities between the supply voltage and the predistorted input produces glitches in the output power [see Fig. 7(c)] and consequent spectral regrowth [see Figs. 7(b) and 8(b)].

As indicated in Table I, the dc power consumption is halved with ML ET, compared with a fixed supply level, for both 1.4- and 10-MHz LTE signals. In this table, $\eta_{D,\mathrm{PA}}$ is the drain efficiency of the outphasing PA, $\eta_{p\mathrm{DAC}}$ is the efficiency of the power-DAC supply modulator, and $\eta_{\mathrm{TOT,SYS}}$ is the total efficiency of the system, $\eta_{\mathrm{TOT,PA}} \times \eta_{p\mathrm{DAC}}$. There is a clear efficiency benefit to ML-CO compared with outphasing only (fixed supply). Although the ML supply modulation causes nonlinearities, as seen in the spectrum plots in Figs. 7(b) and 8(b), DPD is able to restore the linearity of the system as also visible in the AM/AM and AM/PM plots of the linearized system [see Figs. 7(c) and 8(c)].

The presented DPD is not optimized for these wideband communication signals, since the PA has been characterized with Gaussian-like pulses of Fig. 6(a) [30]. Further linearity

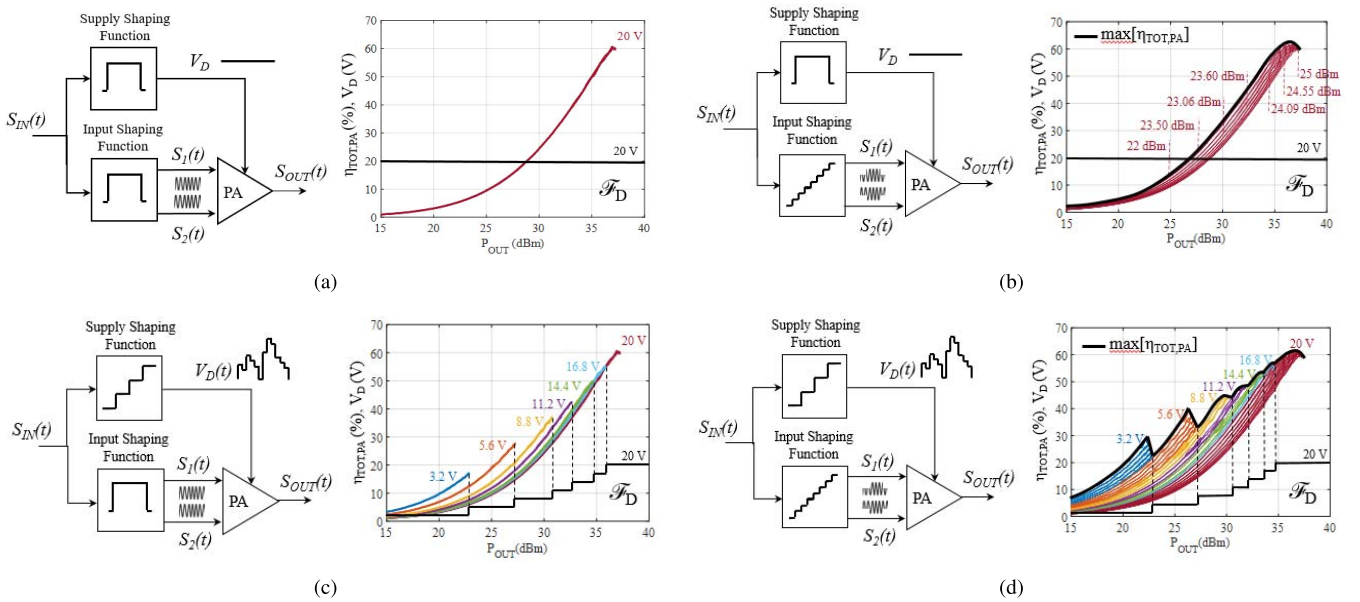

Fig. 9. ML-CO PA control strategies overview. (a) Conventional CO driving technique with fixed input power and supply level. (b) Drive modulation or (c) supply modulation is introduced to enhance back-off efficiency. (d) Both supply and drive modulation are introduced to increase back-off efficiency; the maximum efficiency trajectory is highlighted in the plot.

enhancements can be obtained by employing a feedback loop for the adaptation of the coefficients and a DPD with memory.

III. ML-CO PA Control Strategies

As shown in Table I, when a fixed input power (i.e., 25 dBm or 0.63 W) is used, the total efficiency is significantly decreased compared with the drain efficiency. In this section, we consider the use of alternate control strategies, including input amplitude modulation, and compare the relative benefits in terms of efficiency improvement, system complexity, and linearity. The experimental setup allows for straightforward implementation of different driving techniques.

A. Fixed Input Power/Fixed Supply

The conventional method of driving a CO PA is with fixed-amplitude, phase-modulated signals, as schematically shown in Fig. 9(a). A fixed input power is employed on both branches, and the PA is biased at 20 V. Computation of phase modulation only is required on the transmitter side, and the system complexity is therefore minimized. Linearity is at the best performance with this transmitter architecture and PA, while efficiency for high-PAPR signals can be improved with the following driving techniques.

B. Stepped Input Power/Fixed Supply

One method to enhance backoff efficiency is to reduce the input power at high outphasing angles. This mixed-mode operation [23] has the additional benefit of improving gain at low power levels and extending the dynamic range. To this aim, a characterization at discrete steps, in which a full outphasing angle sweep is performed, provides the efficiency trajectory shown in Fig. 9(b). The input power is varied of 0.5 dB at discrete steps between 22 and 25 dBm (3-dBm variation). Based on this characterization, one could select a continuous input signal modulation trajectory to maximize total efficiency, as qualitatively shown by the plot contour. The efficiency benefits of this driving technique trade off with increased complexity, as this approach requires a transmitter architecture with both amplitude and phase modulation capabilities.

C. Fixed Input Power/Supply Modulation

An alternative approach to improve back-off efficiency is to employ a fixed input power with discrete supply modulation (e.g., power-DAC). This technique is shown qualitatively in Fig. 9(c) and is the method demonstrated in [22]. Fig. 6(a) shows the characterization sequence with such a driving technique. Because the supply is dynamically varied (and hence the trap state of the PAs), a prepulse is introduced to precondition the PA state. The following pulse is used to extract the nonlinear characteristics of the PA for each supply level. The efficiency trajectory and supply shaping table are reported in Fig. 5(a)–(d).

D. Stepped Input Power/Supply Modulation

By comparing the efficiency trajectories of the highest supply level (20 V) in Fig. 9(b) and (c), it is clear that input amplitude modulation provides improved efficiency compared with supply modulation alone. This observation can be extended to the remaining levels by varying the input amplitude in combination with the discrete supply steps.

To this purpose, a characterization sequence like the one shown in Fig. 6(a) is employed, but instead of using a fixed input power at 25 dBm, the same sequence is performed with a measurement pulse with discretized amplitude steps (between 22 and 25 dBm). In this way, multiple efficiency

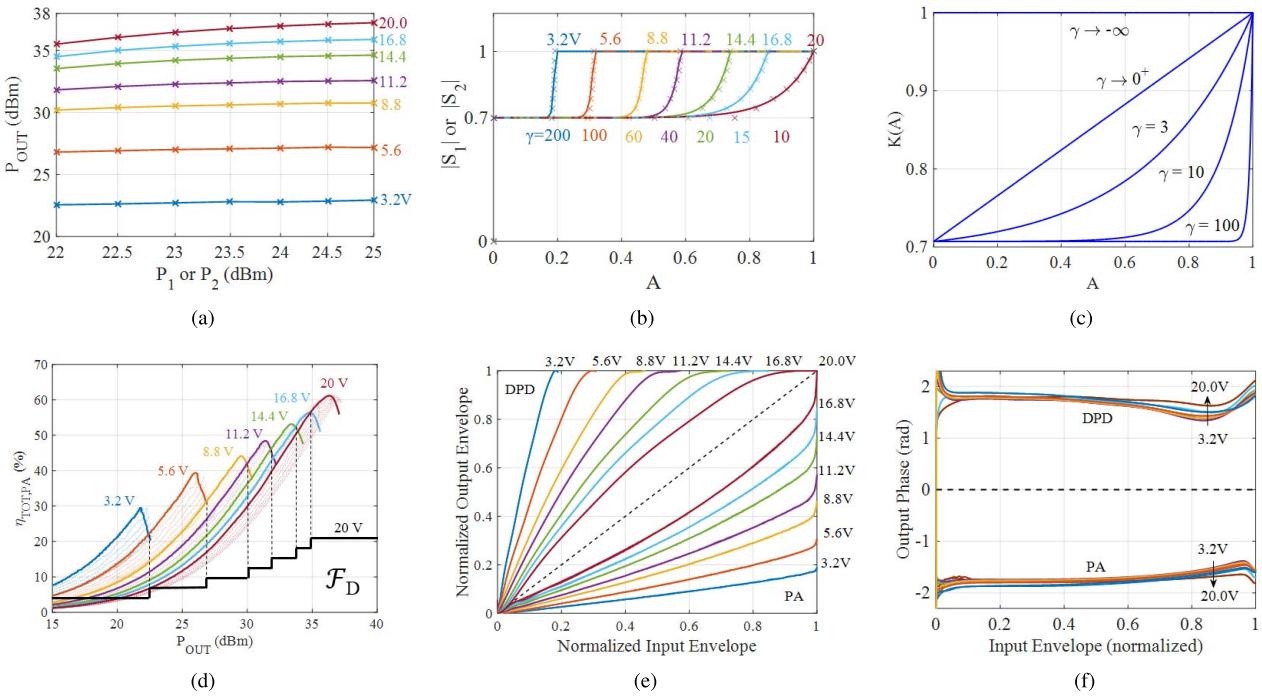

Fig. 10. Significant waveforms for continuous input modulation. (a) By using a stepped pulsed characterization, it is possible to extract the P_{OUT} versus (P_1 or P_2) locus for the maximum efficiency (max[$\eta_{\mathrm{TOT,PA}}$]) of Fig. 9(d). (b) Normalized S_1 and S_2 input envelopes for the maximum efficiency (max[$\eta_{\mathrm{TOT,PA}}$]) of Fig. 9(d). (c) Exponential functions at different γ values used to fit the input envelopes. (d) Superposition of the efficiency with continuous input modulation and with stepped input modulation. (e) AM/AM characteristics. (f) AM/PM characteristics.

characteristics are obtained and superposed in the plots of Fig. 9(d). We note that although discrete steps of input power are used for this characterization, in practice, one would continuously modulate the input drive, as will be described in Section III-E. The maximum efficiency curve is indicated in Fig. 9(d). This approach achieves the highest performance in terms of total efficiency, while system complexity increases and linearity is deteriorated.

E. Continuous Input Modulation/Supply Modulation

If the control strategy with simultaneous input and supply modulation is selected, it is necessary to drive the PA with a continuous signal in order to be able to restore linearity by means of DPD.

The input and output power trajectories that maximize efficiency are shown in Fig. 10(a) for every given supply level. It is worth observing that for low supply voltages, the gain is very low, and therefore, a fixed input power at the minimum (i.e., $P_1 = P_2 = 22$ dBm) can be selected. At higher supply voltages, the gain is increased, and the input power can be shaped with the trajectory shown in the plot. The input and output power trajectories of Fig. 10(a) can be conveniently mapped in terms of normalized envelopes, ($|S_1|$ or $|S_2|$) versus $|S_{\mathrm{IN}}| = A$, as shown in Fig. 10(b). These experimental values can be fit by means of an exponential function as

$$K(A) = \alpha + \beta e^{\gamma A}. \tag{12}$$

The shape of this function is reported in Fig. 10(c) for some significant γ values. The γ parameter is used to arbitrarily set the growth rate of the exponential function. The α and β parameters are employed to limit the $K(A)$ variation within a minimum, K_{MIN}, and a maximum, 1. Therefore, by imposing to (12), the conditions on the minimum ($A = 0$) and on the maximum ($A = 1$) input amplitude

$$\begin{cases} K(0) = K_{\mathrm{MIN}} \\ K(1) = 1 \end{cases} \rightarrow \begin{cases} \alpha = \dfrac{1 - K_{\mathrm{MIN}} e^{\gamma}}{1 - e^{\gamma}} \\ \beta = \dfrac{K_{\mathrm{MIN}} - 1}{1 - e^{\gamma}} \end{cases} \tag{13}$$

the coefficients α and β can be obtained. The γ values can be extracted by fitting the experimental data in Fig. 10(b). However, with the considered MMIC PA, it was not possible to decrease the input power more than 3 dBm due to stability issues in the PA, and thus, the minimum amplitude results in $K_{\mathrm{MIN}} = 1/\sqrt{2}$. This should not be considered as a limitation of the approach, since (12) and (13) could be extended to any input power levels with different K_{MIN} values (e.g., $K_{\mathrm{MIN}} = 0$).

The characterization results using continuous input and supply modulation are reported in Fig. 10(d)–(f). The γ parameters have been individually optimized to fit the input power trajectory for maximum efficiency and their values are reported in Fig. 10(b) (inset).

Continuous input modulation is able to maximize the total efficiency that has been previously extracted with stepped input powers [see Fig. 9(d)]. Total efficiency improves between 9 and 27 percentage points over the whole output power range of the PA. AM/AM and AM/PM characteristics present a remarkably nonlinear behavior compared with the ones

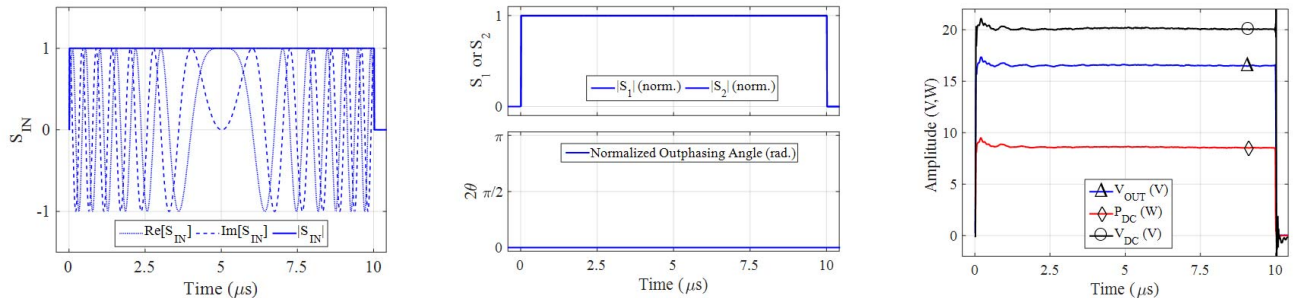

Fig. 11. Exemplifying envelopes for a rectangular RF pulse for radar applications. (a) Input signal S_{IN} with rectangular envelope and 5-MHz linear frequency chirp. (b) PA input signals and normalized outphasing angle. (c) PA supplies and output signal.

extracted with fixed input power [see Fig. 5(c) and (d)] which is, however, compensated with DPD while keeping high efficiency.

F. Special Cases

Two special cases of the proposed exponential function in (12) are worth further note. By substituting (13) into (12), the complete expression of the exponential shaping function can be obtained as

$$K(A) = \frac{1 - K_{\mathrm{MIN}} e^{\gamma}}{1 - e^{\gamma}} + \frac{K_{\mathrm{MIN}} - 1}{1 - e^{\gamma}} e^{\gamma A}. \tag{14}$$

If γ tends to $-\infty$, the exponential function tends to 1

$$\lim_{\gamma \to -\infty} K(A) = 1. \tag{15}$$

This condition corresponds to the driving strategy of Section III-A or III-C with the associated efficiency trajectories.

On the other hand, if γ tends to 0^+, the exponential shaping function degenerates to a linear amplitude shaping between K_{MIN} and 1 with slope $(1 - K_{\mathrm{MIN}})$

$$\lim_{\gamma \to 0^+} K(A) = K_{\mathrm{MIN}} + (1 - K_{\mathrm{MIN}})A. \tag{16}$$

This case can be significant given the reduced computational resources to implement it (i.e., a multiply–accumulate digital block). However, we note that this case will not result in maximum efficiency.

IV. Experimental Results

In this section, we demonstrate the presented ML-CO transmitter capability of efficiently amplify amplitude- and frequency-modulated signals for radar applications. Most radars use rectangular pulses with the transmitter PA operated in strong saturation to maximize output power and efficiency. Since the range resolution depends on the bandwidth of the transmitted signal, a short pulse of duration T increases the range resolution at the expense of ranging capability [31].

Pulse compression techniques aim to overcome this tradeoff by introducing frequency (i.e., chirping) or phase modulation (e.g., BPSK, Barker codes) inside the rectangular pulse [31]. However, this mode of operation with rectangular envelope pulses results in poor spectral characteristics, due to the fast rise time and fall time of the rectangular pulse. Sinclike properties of the rectangular pulse produce a widespread spectrum that could leak into neighboring bands and cause interference with other users or violate regulated spectral masks [27], [31]–[38]. High time sidelobes (-13.2 dB) are also present at the output of the matched filter in the receiver, which can lead to false target triggering. By shaping the pulse envelope before transmitting, it is possible to limit the spectral occupation at the source and obtain low sidelobes at the output of the matched filter in the receiver [27], [31]–[38].

Gaussian-like amplitude-modulated pulses can reduce the time sidelobes and spectral leakage. However, amplitude modulation of the RF pulse envelope highly increases the dissipation in the PA [27], [37], [38], unless the PA supply is modulated to track a highly efficient operative regime [27], [37], [38]. To this aim, we consider test signals, S_{IN}, with a pulse duration of 10 and 100 μs of repetition period [as the characterization sequence depicted in Fig. 6(a)]. The pulse amplitude has been shaped with five different windowing functions typically employed in pulse-compressed radar transmitters [31], [35], [38]: rectangular, Tukey, Hanning, triangular, and Blackman. A linear frequency modulation at 0 (no frequency chirp), 10, and 20 MHz has been applied to the pulse to increase the bandwidth (i.e., radar range resolution) while keeping the same pulse shape and duration [31], [38]. This frequency chirp has been implemented by I/Q modulation as can be appreciated in Figs. 11(a) and 12(a).

The ML-CO PA is characterized with the techniques presented in Section III and DPD is extracted accordingly. Two control strategies are compared.

1) *Fixed Input Power/Fixed Supply:* This is the conventional method of driving a radar PA in which the PA power supply is turned ON and OFF during the pulse duration [27], [37]. This operating mode corresponds to the one discussed in Section III-A where a fixed input power at 25 dBm is used and phase modulation is employed to generate amplitude-modulated signals.
2) *Continuous Input Modulation/Supply Modulation:* This control strategy employs both continuous input and supply modulation to enhance back-off efficiency of amplitude-modulated signals (Section III-E).

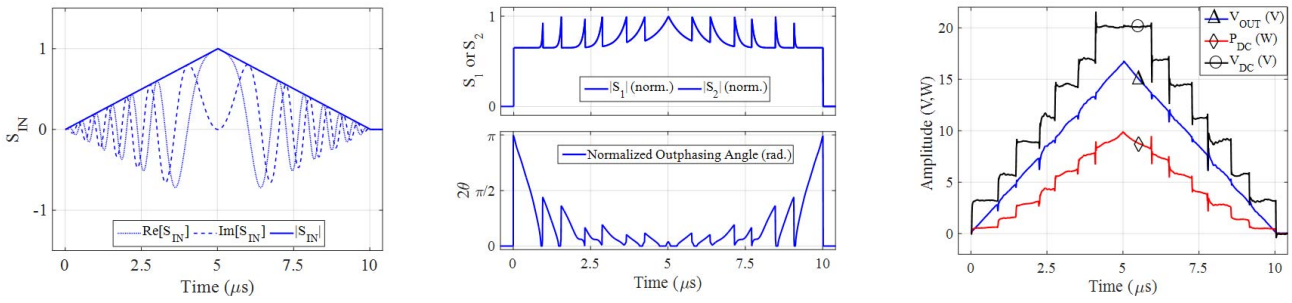

(a) (b) (c)

Fig. 12. Exemplifying envelopes for a triangular RF pulse for radar applications. (a) Input signal S_{IN} with triangular envelope and 5-MHz linear frequency chirp. (b) PA input signals and normalized outphasing angle. (c) PA supplies and output signal.

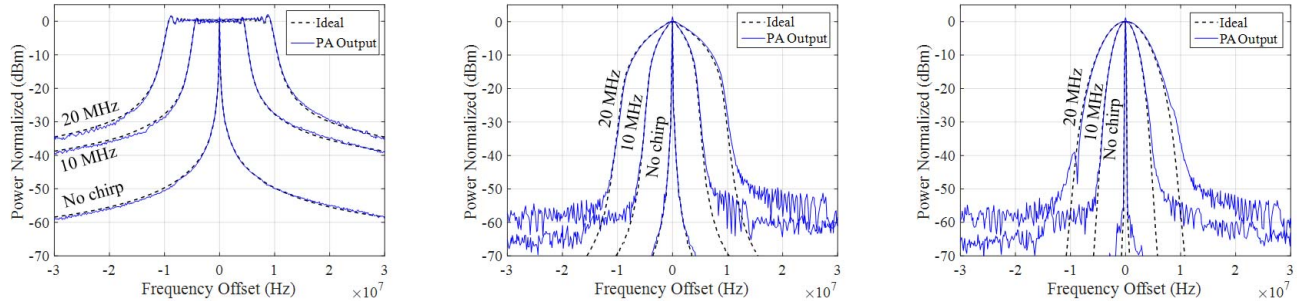

(a) (b) (c)

Fig. 13. Output spectra of the PA with the DPD enabled with three weighting windows. (a) Rectangular. (b) Triangular. (c) Blackman.

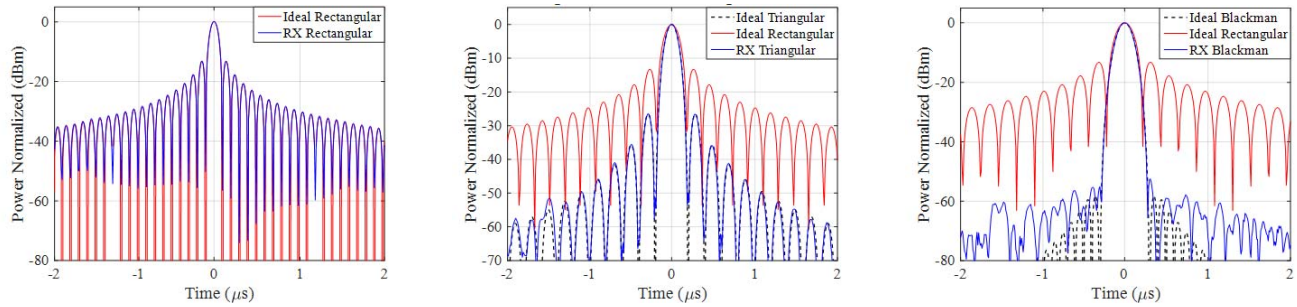

(a) (b) (c)

Fig. 14. Matched filter output in a pulse-compressed radar receiver with linear frequency modulation. (a) Rectangular. (b) Triangular. (c) Blackman.

Time-domain waveforms for a typical radar pulse with rectangular envelope and frequency chirp are provided in Fig. 11. In this case, operating modes 1) and 2) produce the same results, because the PA is operated for a maximum power generation within the pulse. Two constant-envelope $[K(A) = 1]$ outphased input signals, $S_1(t)$ and $S_2(2)$, are generated at digital baseband and unconverted at 9.7 GHz by the bench into the PA input signals, $P_1(t)$ and $P_2(t)$. The measured supply voltage, dc power, and output voltage are shown in the figure. Note that the dc power and thus efficiency are the same for all the considered chirp frequencies, since the output power is the same. The spectrum of the RF output power for the three chirping frequencies is shown in Fig. 13(a). The spectrum of this window function is almost identical to the ideal case, as well as the matched filter output [see Fig. 14(a)].

Fig. 12 shows the waveforms for an RF pulse with triangular amplitude modulation and frequency chirp. In this case, the ML-CO PA efficiency is enhanced by constantly adapting the supply voltage at the drain and by continuously varying the input signal of the two PAs as discussed in Section III-E. The outphasing angle (2θ) is used to perform a fine shaping of the amplitude at the output of the PA in order to produce linear amplification (V_{OUT}) of the input signal S_{IN}. DPD is able to restore linearity of the system. Output spectra for three chirp frequencies 0 (no chirp), 10, and 20 MHz are shown in Fig. 13(b), and the matched filter output is shown in Fig. 14(b).

A comparative overview of the control strategies 1) and 2) is reported in Table II with a selection of typical amplitude tapers for radar transmitters. The rectangular pulse reaches

TABLE II
PERFORMANCE SUMMARY WITH DIFFERENT CONTROL STRATEGIES AND PULSE WAVEFORMS FOR RADAR APPLICATIONS

Amplitude Taper (PAPR)	Control Strategy	-3 dB Bandwidth f_{LFM}=0 MHz	-3 dB Bandwidth f_{LFM}=20 MHz	1st Time Sidelobe	$P_{OUT,PA}$	$P_{IN,PA}$	$\eta_{TOT,PA}$	η_{pDAC}	$\eta_{TOT,SYS}$
Rectangular (0 dB)	**Fixed Input Fixed Supply**	**90 kHz**	**19.4 MHz**	**-13.2 dB**	**5.51 W 37.41 dBm**	**0.63 W 28.00 dBm**	**59.2%**	-	**59.2%**
Tukey r=0.5 (1.6 dB)	Fixed Input Fixed Supply	116 kHz	13.9 MHz	-15.1 dB	3.50 W 35.44 dBm	0.63 W 28.00 dBm	46.1%	-	46.1%
Tukey r=0.5 (1.6 dB)	**Cont. Input Supply Mod.**	**116 kHz**	**13.8 MHz**	**-15.0 dB**	**3.45 W 35.38 dBm**	**0.52 W 27.13 dBm**	**49.1%**	**95%**	**46.7%**
Hanning (4.3 dB)	Fixed Input Fixed Supply	144 kHz	7.6 MHz	-31.1 dB (ideal -31.5 dB)	1.94 W 32.88 dBm	0.63 W 28.00 dBm	32.6%	-	32.6%
Hanning (4.3 dB)	**Cont. Input Supply Mod.**	**144 kHz**	**7.6 MHz**	**-30.4 dB (ideal -31.5 dB)**	**2.10 W 33.23 dBm**	**0.40 W 26.03 dBm**	**44.4%**	**95%**	**42.2%**
Triangular (4.8 dB)	Fixed Input Fixed Supply	126 kHz	6.6 MHz	-26.6 dB	1.74 W 32.41 dBm	0.63 W 28.00 dBm	30.5%	-	30.5%
Triangular (4.8 dB)	**Cont. Input Supply Mod.**	**126 kHz**	**6.6 MHz**	**-26.6 dB**	**1.90 W 32.80 dBm**	**0.37 W 25.67 dBm**	**39.1%**	**95%**	**37.1%**
Blackman (5.2 dB)	Fixed Input Fixed Supply	162 kHz	6.0 MHz	-52.5 dB (ideal -58.2 dB)	1.58 W 31.99 dBm	0.63 W 28.00 dBm	28.1%	-	28.1%
Blackman (5.2 dB)	**Cont. Input Supply Mod.**	**162 kHz**	**6.0 MHz**	**-42.4 dB (ideal -58.2 dB)**	**1.69 W 32.28 dBm**	**0.38 W 25.81 dBm**	**42.0%**	**95%**	**39.9%**

the highest efficiency with 59.2% and the widest bandwidth of 19.4 MHz, but this comes with very high first sidelobe level (−13.2 dB) at the output of the matched filter and a slow roll-off in the spectrum decay. By tapering the pulse envelope with a weighting window, it is possible to reduce the temporal sidelobes up to −42.4 dB, with the Blackman window [see Figs. 13(c) and 14(c)], and reduce the spectral occupation significantly compared with the rectangular chirped pulse. The efficiency improvement with supply modulation with respect to a pulsed rectangular supply is up to 11.8 percentage points.

V. CONCLUSION

This paper presents, for the first time, the application of ML supply modulation of a CO PA driven with a novel control strategy based on continuous input modulation. In the ML-CO technique, the advantages of ET and outphasing architectures are combined in order to provide efficient and linear amplification of high PAPR signals. ET is limited to discrete levels and outphasing is employed for fine amplitude control.

Beyond the results of the related conference paper, this paper presents a detailed investigation of ML-CO control strategies, including combination of discrete supply modulation, stepped input power, and continuous input modulation. Similar to the supply shaping function in ET, an input amplitude shaping is introduced to maximize intralevel efficiency in the ML-CO PA.

The linearized ML-CO PA is demonstrated with fixed input power for a 9.3-dB PAPR, 1.4-MHz LTE signal and with an 11.3-dB PAPR, 10-MHz LTE signal both centered at 9.7 GHz. For both signals, the average total power consumption is reduced by a factor of two when supply modulation is used.

Pulsed characterization is also used to identify an optimal efficiency trajectory, which can be tracked by continuously varying the input power in the ML-CO PA. A simple exponential function has been identified and capable to track this optimal efficiency trajectory. By using continuous input modulation and supply modulation jointly, the total efficiency of the ML-CO improves between 9 and 27 percentage points over the all output power range of the PA.

The overall control strategy has been demonstrated with advanced radar waveforms with amplitude shaping and frequency modulation. The presented ML-CO PA is capable to efficiently generate (59.2%) a rectangular pulse with up to 19.4-MHz bandwidth and −13.2 dB first time sidelobe. Lower temporal sidelobes (up to −42.4 dB) can be achieved with Gaussian-like amplitude tapers (i.e., Hanning and Blackman), while efficiency is improved up to 11.8 percentage points compared with the fixed input/fixed supply case.

ACKNOWLEDGMENT

The authors would like to thank National Instruments for invaluable instrumentation and other support, especially Dr. M. V. Bossche and F. Signorini.

REFERENCES

[1] W. H. Doherty, "A new high efficiency power amplifier for modulated waves," in *Proc. IRE*, vol. 24, no. 9, pp. 1163–1182, Sep. 1936.

[2] W. Hallberg, M. Özen, D. Gustafsson, K. Buisman, and C. Fager, "A Doherty power amplifier design method for improved efficiency and linearity," *IEEE Trans. Microw. Theory Techn.*, vol. 64, no. 12, pp. 4491–4504, Dec. 2016.

[3] M. J. Pelk, W. C. E. Neo, J. R. Gajadharsing, R. S. Pengelly, and L. C. N. D. Vreede, "A high-efficiency 100-W GaN three-way Doherty amplifier for base-station applications," *IEEE Trans. Microw. Theory Techn.*, vol. 56, no. 7, pp. 1582–1591, Jul. 2008.

[4] A. Grebennikov, "A high-efficiency 100-W four-stage Doherty GaN HEMT power amplifier module for WCDMA systems," in *IEEE MTT-S Int. Microw. Symp. Dig.*, Jun. 2011, pp. 1–4.
[5] X. Moronval and J. Gajadharsing, "A 100 W multi-band four-way integrated Doherty amplifier," in *IEEE MTT-S Int. Microw. Symp. Dig.*, May 2016, pp. 1–3.
[6] E. McCune, "Operating modes of dynamic power supply transmitter amplifiers," *IEEE Trans. Microw. Theory Techn.*, vol. 62, no. 11, pp. 2511–2517, Nov. 2014.
[7] M. Olavsbråten and D. Gecan, "Bandwidth reduction for supply modulated RF pas using power envelope tracking," *IEEE Microw. Wireless Compon. Lett.*, vol. 27, no. 4, pp. 374–376, Apr. 2017.
[8] S. S. Modi, P. T. Balsara, and O. E. Eliezer, "Reduced bandwidth class H supply modulation for wideband RF power amplifiers," in *Proc. IEEE 13th Annu. Wireless Microw. Technol. Conf. (WAMICON)*, Apr. 2012, pp. 1–7.
[9] H. Chireix, "High power outphasing modulation," *Proc. IRE*, vol. 23, no. 11, pp. 1370–1392, Nov. 1935.
[10] D. J. Perreault, "A new power combining and outphasing modulation system for high-efficiency power amplification," in *Proc. 53rd IEEE Int. Midwest Symp. Circuits Syst.*, Aug. 2010, pp. 441–444.
[11] T. W. Barton, A. S. Jurkov, P. H. Pednekar, and D. J. Perreault, "Multi-way lossless outphasing system based on an all-transmission-line combiner," *IEEE Trans. Microw. Theory Techn.*, vol. 64, no. 4, pp. 1313–1326, Apr. 2016.
[12] M. Litchfield, T. Cappello, C. Florian, and Z. Popovic, "X-band GaN multi-level chireix outphasing PA with a discrete supply modulator MMIC," in *Proc. IEEE Compound Semiconductor IC Symp.*, Oct. 2016, pp. 138–141.
[13] J. Jeong, D. F. Kimball, M. Kwak, C. Hsia, P. Draxler, and P. M. Asbeck, "Wideband envelope tracking power amplifiers with reduced bandwidth power supply waveforms and adaptive digital predistortion techniques," *IEEE Trans. Microw. Theory Techn.*, vol. 57, no. 12, pp. 3307–3314, Dec. 2009.
[14] H. Cao, C. Fager, T. Khan, A. S. Tehrani, and T. Eriksson, "Comparison of bandwidth reduction schemes in dynamic load modulation power amplifier architectures," in *Proc. Workshop Integr. Nonlinear Microw. Millim.-Wave Circuits (INMMIC)*, Apr. 2011, pp. 1–4.
[15] C. Florian, T. Cappello, R. P. Paganelli, D. Niessen, and F. Filicori, "Envelope tracking of an RF high power amplifier with an 8-level digitally controlled GaN-on-Si supply modulator," *IEEE Trans. Microw. Theory Techn.*, vol. 63, no. 8, pp. 2589–2602, Aug. 2015.
[16] N. Wolff, W. Heinrich, and O. Bengtsson, "100-MHz GaN-HEMT class-G supply modulator for high-power envelope-tracking applications," *IEEE Trans. Microw. Theory Techn.*, vol. 65, no. 3, pp. 872–880, Mar. 2017.
[17] K. Mimis and G. T. Watkins, "A reactively load-modulated RF low-power amplifier with multilevel supply voltage for multi-standard RF front-ends," in *Proc. GeMiC German Microw. Conf.*, Mar. 2014, pp. 1–4.
[18] G. Lasser, M. Duffy, M. Olavsbråten, and Z. Popovic, "Gate control of a two-stage GaN MMIC amplifier for amplitude and phase linearization," in *Proc. IEEE 18th Wireless Microw. Technol. Conf. (WAMICON)*, Apr. 2017, pp. 1–5.
[19] J. Hur, K.-W. Kim, O. Lee, C.-H. Cho, K. Lim, and J. Laskar, "Highly efficient and linear level shifting digital LINC transmitter with a phase offset cancellation," in *Proc. IEEE Radio Wireless Symp.*, Jan. 2009, pp. 211–214.
[20] P. A. Godoy, S. Chung, T. W. Barton, D. J. Perreault, and J. L. Dawson, "A 2.4-GHz, 27-dBm asymmetric multilevel outphasing power amplifier in 65-nm CMOS," *IEEE J. Solid-State Circuits*, vol. 47, no. 10, pp. 2372–2384, Oct. 2012.
[21] C. Xie and A. Walker, "A digitally optimum driven X-band outphasing power amplifier," in *Proc. GOMACTech*, Mar. 2016, pp. 43–44.
[22] T. Cappello, C. Florian, T. W. Barton, M. Litchfield, and Z. Popovic, "Multi-level supply-modulated chireix outphasing for lte signals," in *IEEE MTT-S Int. Microw. Symp. Dig.*, Jun. 2017, pp. 1–4.
[23] J. H. Qureshi *et al.*, "A 90-w peak power gan outphasing amplifier with optimum input signal conditioning," *IEEE Trans. Microw. Theory Techn.*, vol. 57, no. 8, pp. 1925–1935, Aug. 2009.
[24] T. W. Barton and D. J. Perreault, "Theory and implementation of RF-input outphasing power amplification," *IEEE Trans. Microw. Theory Techn.*, vol. 63, no. 12, pp. 4273–4283, Dec. 2015.
[25] Y. Tajima, D. Wandrei, Q. S. Schultz, T. Quach, P. Watson, and W. Gouty, "Improved efficiency in outphasing power amplifier by mixing outphasing and amplitude modulation," in *Proc. IEEE Topical Conf. RF/Microw. Power Model. Radio Wireless Appl. (PAWR)*, Jan. 2017, pp. 55–58.
[26] M. Litchfield and Z. Popovic, "Multi-level Chireix outphasing GaN MMIC PA," in *Proc. IEEE Compound Semiconductor Integr. Circuit Symp.*, Oct. 2015, pp. 1–4.
[27] C. Florian, T. Cappello, D. Niessen, R. P. Paganelli, S. Schafer, and Z. Popovic, "Efficient programmable pulse shaping for *X*-band GaN MMIC radar power amplifiers," *IEEE Trans. Microw. Theory Techn.*, vol. 65, no. 3, pp. 881–891, Mar. 2017.
[28] T. Cappello, A. Santarelli, and C. Florian, "Dynamic RON characterization technique for the evaluation of thermal and off-state voltage stress of GaN switches," *IEEE Trans. Power Electron.*, to be published.
[29] C. Florian, D. Niessen, T. Cappello, A. Santarelli, F. Filicori, and Z. Popovic, "Pre-pulsing characterization of gan pas with dynamic supply," in *IEEE MTT-S Int. Microw. Symp. Dig.*, May 2016, pp. 1–4.
[30] C. Florian, T. Cappello, A. Santarelli, D. Niessen, F. Filicori, and Z. Popovic, "A pre-pulsing technique for the characterization of GaN power amplifiers with dynamic supply under controlled thermal and trapping states," *IEEE Trans. Microw. Theory Techn.*, to be published.
[31] N. Levanov and E. Mozeson, *Radar Signals*. Hoboken, NJ, USA: Wiley, 2004, ch. 4.
[32] R. Chen and B. Cantrell, "Highly bandlimited radar signals," in *Proc. IEEE Radar Conf.*, Apr. 2002, pp. 220–226.
[33] H. H. Faust, B. Connolly, T. M. Firestone, R. C. Chen, B. H. Cantrell, and E. L. Mokole, "A spectrally clean transmitting system for solid-state phased-array radars," in *Proc. IEEE Radar Conf.*, Apr. 2004, pp. 140–144.
[34] J. D. Graaf, H. Faust, J. Alatishe, and S. Talapatra, "Generation of spectrally confined transmitted radar waveforms: Experimental results," in *Proc. IEEE Conf. Radar*, Apr. 2006, p. 8.
[35] C. Baylis *et al.*, "Designing for spectral conformity: Issues in power amplifier design," in *Proc. Int. Waveform Diversity Design Conf.*, Aug. 2010, pp. 000-220–000-223.
[36] C. Baylis, M. Fellows, L. Cohen, and R. J. Marks, "Solving the spectrum crisis: Intelligent, reconfigurable microwave transmitter amplifiers for cognitive radar," *IEEE Microw. Mag.*, vol. 15, no. 5, pp. 94–107, Jul. 2014.
[37] G. van der Bent *et al.*, "A 10 watt S-band MMIC power amplifier with integrated 100 MHz switch-mode power supply and control circuitry for active electronically scanned arrays," *IEEE J. Solid-State Circuits*, vol. 48, no. 10, pp. 2285–2295, Oct. 2013.
[38] A. Zai, M. Pinto, M. Coffey, and Z. Popovic, "Supply-modulated radar transmitters with amplitude-modulated pulses," *IEEE Trans. Microw. Theory Techn.*, vol. 63, no. 9, pp. 2953–2964, Sep. 2015.

Tommaso Cappello (S'13–M'17) received the Laurea (*cum laude*) degree in electrical engineering and Ph.D. degree from the University of Bologna, Bologna, Italy, in 2013 and 2017, respectively.

Since 2017, he has been with the Microwave and RF Research Group, University of Colorado Boulder, Boulder, CO, USA. His current research interests include power electronics, RF electronics, and digital signal processing techniques for high-efficiency transmitter applications.

Taylor W. Barton (S'07–M'12) received the B.Sc. and M.Eng. degrees in electrical engineering and D.Sc. degrees from the Massachusetts Institute of Technology (MIT), Cambridge, MA, USA.

She was a Post-Doctoral Associate with the MIT Microsystems Technology Laboratories until 2014 and then became an Assistant Professor with the University of Texas at Dallas, Richardson, TX, USA. In 2016, she joined the Department of Electrical, Computer, and Energy Engineering, University of Colorado Boulder, Boulder, CO, USA, where she is currently an Assistant Professor and holds the Lockheed Martin Faculty Fellowship for outstanding junior faculty. Her current research interests include high-efficiency RF, power, and analog circuit design.

Corrado Florian (S'02–M'04) received the Ph.D. degree in electronics from the University of Bologna, Bologna, Italy, in 2004.

Since 2006, he has been a Research Associate with the Department of Electrical, Electronic and Information Engineering, University of Bologna, where he is currently a Lecturer of power electronics and RF electronics courses. His current research interests include RF and microwave circuit, power electronics, microwave and power device characterization, and modeling.

Michael Litchfield (S'12–M'16) received the B.S.E.E. degree from the University of New Hampshire, Durham, NH, USA, in 2011, and the M.S.E.E. and Ph.D. degrees from the University of Colorado, Boulder, CO, USA, in 2014 and 2016, respectively.

In 2011, he joined Mercury Systems, Salem, NH, USA, where he designed quadrature upconverter/downconverter modules for a DRFM system. He is currently with Technology Solutions, BAE Systems, Nashua, NH, USA, where he is involved in wideband high-power GaN MMIC PA design and nonlinear transistor model development.

Zoya Popovic (S'86–M'90–SM'99–F'02) received the Dipl.Ing. degree from the University of Belgrade, Belgrade, Serbia, and the Ph.D. degree from the California Institute of Technology, Pasadena, CA, USA.

In 2001 and 2003, she joined the Technical University of Munich, Munich, Germany, as a Visiting Professor. In 2014, she joined ISAE, Toulouse, France, as a Visiting Professor. She is currently a Distinguished Professor and the Lockheed Martin Endowed Chair of Electrical Engineering with the University of Colorado Boulder, Boulder, CO, USA. She has graduated 56 Ph.Ds. and currently advises 12 doctoral students. Her current research interests include high-efficiency power amplifiers and transmitters, microwave and millimeter-wave high-performance circuits for communications and radar, medical applications of microwaves, millimeter-wave and THz quasi-optical techniques, and wireless powering.

Dr. Popovic was a recipient of two IEEE MTT-S Microwave Prizes for best journal papers, the White House NSF Presidential Faculty Fellow Award, the URSI Issac Koga Gold Medal, the ASEE/HP Terman Medal, and the German Humboldt Research Award. She was elected as Foreign Member of the Serbian Academy of Sciences and Arts in 2006. She was named the IEEE MTT-S Distinguished Educator in 2013 and the University of Colorado Distinguished Research Lecturer in 2015.